PERGAMON

Quaternary Science Reviews 21 (2002) 361–376

QSR

Estimating past continental ice volume from sea-level data

Glenn A. Milne[a,*], Jerry X. Mitrovica[b], Daniel P. Schrag[c]

[a] Department of Geological Sciences, University of Durham, Durham DH1 3LE, UK
[b] Department of Physics, University of Toronto, 60 St. George Street, Toronto Ont., Canada M5S 1A7
[c] Department of Earth and Planetary Sciences, Harvard University, 20 Oxford Street, Cambridge, MA 02138, USA

Received 1 March 2001; accepted 15 September 2001

Abstract

We predict sea-level change since the Last Glacial Maximum (LGM) at four far-field sites (Barbados, Bonaparte Gulf, Huon Peninsula and Tahiti) using a revised theoretical formalism. This formalism includes a time-varying shoreline geometry, an accurate treatment of sea-level variations near regions of ice retreat and the influence of glacial cycle perturbations in Earth rotation. We elucidate the physics of far-field sea-level change by de-constructing the predicted signal into spatially uniform versus spatially varying components, as well as isolating contributions due to the ice load, the ocean load and the rotational potential. We demonstrate that the sum of these three contributions plus the spatially uniform sea-level fall associated the with retreat of grounded marine ice sheets can produce a significant difference between predictions of sea-level change at far-field sites and the eustatic (or meltwater) curve associated with the adopted ice model. This difference is site and time dependent. For example, the total sea-level rise since the LGM predicted using our ice–earth model can be either smaller (e.g., Barbados) or larger (e.g., Tahiti) than the eustatic sea-level change. Finally, we review procedures that have been applied to estimate continental ice volume from far-field sea-level observations and apply these procedures to data from Barbados and Bonaparte Gulf. Applying an ice-earth model that is tuned to fit the Barbados data, we estimate a change in grounded ice volume from the LGM to the present of $43.5–51 \times 10^6\,km^3$ based on Barbados data and an LGM ice volume estimate of $51 \times 10^6\,km^3$ based on Bonaparte Gulf data. Our results for the Bonaparte Gulf data are consistent with the recent study by Yokoyama et al. (Nature 406 (2000) 713). These LGM ice volume estimates map into a eustatic (or meltwater) sea-level rise of 115–135 m. Taking into account plausible variations in the adopted radial earth model introduces uncertainties in the range of $\pm 1.5 \times 10^6\,km^3$ for ice volume estimates based on the Barbados data.

1. Introduction

The level of the oceans relative to the land has changed dramatically over the past ~20 ka due to the melting of the last great ice sheets (e.g., Jamieson, 1865; Daly, 1925; Bloom, 1967; Walcott, 1972; Chappell, 1974; Farrell and Clark, 1976; Peltier and Andrews, 1976). A global distribution of sea-level observations (e.g., Pirazolli, 1991) shows that the magnitude and temporal form of sea-level change varies significantly with geographic location relative to the major centers of glaciation. For example, sea-level changes in regions once glaciated (so-called 'near-field' regions) are characterized by a monotonic fall over most, if not all, of the period during which they have been ice free. On the other hand, sea-level records from sites distant from major glacial activity (so-called 'far-field' sites) display a monotonic sea-level rise during the period of major deglaciation.

The magnitude and spatial extent of the ice–water mass exchange during a glacial cycle is sufficient to produce a significant deformation of the solid Earth which proceeds until a state of isostatic equilibrium is reached. The surface mass flux and the associated solid earth response are commonly described by the general term glacial isostatic adjustment, hereafter abbreviated to GIA. In near-field regions, for example, the uplift of the solid surface during and following ice load removal is the dominant process resulting in a sea-level fall of up to several hundreds of meters from the Last Glacial Maximum (LGM) to the present. In contrast, the addition of glacial meltwater to the global oceans is the dominant contribution to the observed sea-level rise in far-field regions. (Note that meltwater derived from

*Corresponding author. Tel.: +44-191-374-2512; fax: +44-191-374-2510.
E-mail address: g.a.milne@durham.ac.uk (G.A. Milne).

0277-3791/02/$ - see front matter
PII: S0277-3791(01)00108-1

floating ice will not produce a sea-level change and so we will use the term meltwater in connection with grounded ice only.) These examples are, of course, end members of the global sea-level response. At sites where these two components of the GIA sea-level contribution are similar in magnitude, a more complex, non-monotomic signal is observed (e.g., Shennan et al., 1995).

Relative sea-level variations associated with GIA are driven by a number of mechanisms (e.g., Farrell and Clark, 1976). The end-member cases described above illustrate that the relative magnitudes of these mechanisms determine the spatial and temporal form of the GIA-induced sea-level response. In general, near-field data are most sensitive to the ice-load induced deformation. For this reason, these data have commonly been employed to constrain the rheological properties of the Earth as well as the spatial and temporal evolution of the Late Pleistocene ice cover (e.g., Haskell, 1935; Vening Meinesz, 1937; Wu and Peltier, 1983; Tushingham and Peltier, 1991; Lambeck, 1993; Mitrovica, 1996; Lambeck et al., 1998). Far-field data, in contrast, are more sensitive to the rate and magnitude of meltwater input to the oceans during deglaciation. These data therefore provide a more robust measure of the meltwater signal, which can be interpreted as the excess ice volume existing on the Earth's surface at some past time relative to the volume at present (e.g., Nakada and Lambeck, 1989; Peltier, 1994; Flemming et al., 1998; Yokoyama et al., 2000). In fact, these data provide the most direct measure of the total mass exchanged between grounded ice and the oceans during the last glacial cycle (e.g., Clark and Mix, 2000).

The different applications of sea-level data are of interest to a variety of earth scientists. For example, the constraints provided by near-field data on the spatial and temporal distribution of ice in different regions can be used alongside information obtained from glacial geology and glaciology research to produce improved reconstructions of ice sheet histories. The application of far-field sea-level data to infer meltwater influx (and thus past total ice volume) is of interest to both glacial geologists and glaciologists, as a bound on the integrated ice volume existing on the Earth's surface at any time, as well as geochemists and paleoceanographers who are interested in the total mass of grounded ice during the last glacial maximum (LGM) to help interpret the oxygen isotope record of sea water recorded in deep ocean sediments. The interest of such a broad range of earth scientists to this application of far-field sea-level data has motivated the main goal of this paper: to review and clarify the mapping between glacial cycle ice mass variations and far-field sea-level observations. This aim is particularly relevant given the increasing complexity of GIA-based sea-level modeling and the inconsistent use of terminology, both of which have led to some confusion in the interpretation of far-field sea-level observations.

To achieve the above goal we first review, in Section 2.1, the current theory of GIA-induced sea-level change. This discussion includes recent advances such as the incorporation of earth rotation (e.g., Han and Wahr, 1989; Milne and Mitrovica, 1996, 1998a) and the accurate simulation of sea-level change in the vicinity of marine-based ice sheets (e.g., Milne, 1998; Milne et al., 1999). In Section 2.2, we apply the theory reviewed in Section 2.1 and show predictions of sea-level change at four far-field sites where data have been collected (Barbados, Bonaparte Gulf, Huon Peninsula and Tahiti). In particular, we de-construct the predicted total signal at each of these sites into the different components discussed in Sections 2.1 and 2.2.

In Section 3 we describe the procedure for estimating the magnitude of ice-ocean mass flux from sea-level data, and provide estimates of the reduction in ice volume from the LGM to the present based on two independent data sets. We also consider and quantify some sources of uncertainty associated with the inference procedure. A summary of our main results is given in Section 4.

2. Modeling GIA-induced sea-level change

2.1. Sea-level theory

First, let us define the term 'sea level' as the vertical height difference between the equilibrium ocean surface, or geoid, and the Earth's solid surface. Any relative vertical motion between these two surfaces will contribute to a change in sea level. This general relationship can be expressed quantitatively as

$$S(\theta,\psi,t) = C(\theta,\psi)[G(\theta,\psi,t) - R(\theta,\psi,t)], \quad (1)$$

where $S(\theta,\psi,t)$ describes a change in sea level between a zero reference time (such as the beginning of the last glacial cycle) and a later time t at a geographic location with colatitude θ and east longitude ψ. $G(\theta,\psi,t)$ and $R(\theta,\psi,t)$ define the vertical perturbations to the geoid and the solid surface, respectively, and $C(\theta,\psi)$ is the so-called ocean function which is assigned the value of unity in ocean regions and the value of zero in continental regions (Munk and MacDonald, 1960). It is assumed in Eq. (1) that the shoreline location does not vary with time. The extension of theory required to weaken this constraint is described below.

To accurately predict changes in sea level associated with any geodynamic phenomenon, the physical mechanisms that contribute to the fields G and R in Eq. (1) must first be identified. A significant body of work exists that considers the influence of GIA on sea level (e.g., Woodward, 1888; Daly, 1925; Bloom, 1967; Walcott,

1972; Chappell, 1974; Farrell and Clark, 1976; Peltier and Andrews, 1976; Clark et al., 1978; Wu and Peltier, 1983; Nakada and Lambeck, 1987; Mitrovica and Peltier, 1991; Johnston, 1993; Milne, 1998). An in-depth historical review of this literature is beyond the scope of this paper and, instead, we focus our discussion on outlining the key GIA-related mechanisms that contribute to sea-level change. This discussion will act as a primer for the far-field sea-level predictions presented in Section 2.2.

We consider first the influence of the surface mass redistribution on sea level. The GIA-related surface loading is comprised of two principal components: the Late Pleistocene ice sheet histories and the associated sea-level change, $S(\theta,\psi,t)$. The total surface load, $L(\theta,\psi,t)$, is commonly written as

$$L(\theta,\psi,t) = \rho_{\mathrm{I}} I(\theta,\psi,t) + \rho_{\mathrm{W}} S(\theta,\psi,t), \tag{2}$$

where ρ_{I} and ρ_{W} are the densities of ice and water, respectively. $I(\theta,\psi,t)$ is the change in height of ice between a zero reference time and t. Ice shelves that are not grounded do not load the Earth's surface and so are not included in the ice load function $I(\theta,\psi,t)$. Clearly, uncertainties in the ice sheet histories will be a source of error in predictions of GIA-induced sea-level change.

To compute the effect of this surface load on sea level, the internal rheological and density structure of the Earth are required. The characteristic time scales of the surface load expressed in Eq. (2) (100s to 1000s of years) excite both an elastic and non-elastic deformational response of the planet, and the simplest rheological model that incorporates both these responses is a Maxwell solid. (The mechanical analogue for this rheology is a Hookean spring in series with a linear viscous dashpot.) The Maxwell rheology is by far the most commonly adopted in GIA modeling studies. The radial (i.e., depth dependent) density and elastic structure of the Earth have been determined to a relatively high degree of accuracy using seismic methods (e.g., Dziewonski and Anderson, 1981). The viscous structure of the Earth is, in contrast, more poorly constrained. Indeed, analysis of the observational record related to GIA is one of the principle methods available for estimating the viscous structure of the mantle (see discussion in the Introduction).

The vertical deformation of the solid surface can be computed by convolving in space and time the surface load, $L(\theta,\psi,t)$, with the so-called viscoelastic impulse response Green's function for radial displacement (Peltier, 1974). This function defines the vertical surface deformation of a spherically symmetric Maxwell viscoelastic earth model to a surface load that is point-like in space and time. One can consider the surface load due to GIA as being composed of a large number of such 'impulse' loads and so the deformational response to a general load can be expressed as a sum of impulse responses (e.g., Peltier and Andrews, 1976; Clark et al., 1978). To keep the mathematical complexity to a minimum, we write this convolution in the following short-hand form,

$$R^{\mathrm{L}}(\theta,\psi,t) = L(\theta,\psi,t) * \mathrm{GF}^{\mathrm{R,L}}(\theta,\psi,t), \tag{3}$$

where the * denotes convolution in space and time. $R^{\mathrm{L}}(\theta,\psi,t)$ is the radial deformation of the solid surface due to surface mass loading (hence the superscript L). The Green's function is denoted by $\mathrm{GF}^{\mathrm{R,L}}(\theta,\psi,t)$ and the superscript R indicates that this function relates to the radial deformation of the solid surface.

The rheology and density structure of the earth model are embedded within the Green's function. Any assumptions regarding the type of rheology and the spatial variation of viscoelastic properties within the model (commonly assumed to be depth dependent only) will introduce a further degree of inaccuracy to the prediction.

We next consider the effect of surface mass variations on the geoid. When unperturbed by tides and pressure gradients in the atmosphere and ocean, the ocean surface must lie on an equipotential of the Earth's gravity field, and so vertical deflections of this surface are related to perturbations in the Earth's surface gravitational potential. For example, the geopotential will be raised in the vicinity of a large ice sheet due to the direct gravitational attraction between the ice and the ocean water. Of course, the ice sheet will deform the solid earth and the associated, internal, mass redistribution will also perturb the geopotential. The deflection of the geoid associated with the direct attraction of the surface mass load is conventionally termed the "direct effect", whereas the geoid perturbation related to the surface load-induced deformation (or internal mass flux) is termed the "indirect effect".

The vertical perturbation to the geopotential produced by the surface loading can be computed in a manner analogous to Eq. (3):

$$\Phi^{\mathrm{L}}(\theta,\psi,t) = L(\theta,\psi,t) * \mathrm{GF}^{\Phi,\mathrm{L}}(\theta,\psi,t), \tag{4}$$

where Φ^{L} is the load-induced deformation of the geopotential on the undeformed solid surface and $\mathrm{GF}^{\Phi,\mathrm{L}}(\theta,\psi,t)$ is the impulse response Green's function for the geopotential perturbation. If the geoid were to remain on the same equipotential during a glacial cycle, the corresponding geoid height shift would be given by $\Phi^{\mathrm{L}}(\theta,\psi,t)/g$ (to first order), where g is the surface gravitational acceleration. However, the mean ocean surface falls during a period of glaciation and rises during a period of deglaciation. That is, the height of the geoid relative to the solid surface depends on the volume of water occupying the Earth's oceans at any time. (Furthermore, adjustments of the ocean surface also occur in consequence of glaciation-induced deformations of the ocean floor). To first order, this contribution

to the geoid height shift is spatially uniform and is determined by ensuring that the volume of ocean water associated with the predicted sea-level change, $S(\theta,\psi,t)$, is consistent with the ice-ocean mass flux delivered by the adopted ice model. This aspect of the model is discussed in detail below.

The ice–water surface mass redistribution is the most important GIA forcing that contributes to sea-level variations. A secondary forcing arises due to perturbations of the Earth's inertia tensor caused by the surface mass flux and the consequent deformation. This perturbation results in a small change in the Earth's rotation vector which acts to deform the geoid and the solid surface (e.g., Han and Wahr, 1989; Milne and Mitrovica 1996, 1998a; Bills and James, 1996).

The deformation of the ocean bounding surfaces produced by the time-varying centrifugal potential (henceforth the 'rotational potential') can also be calculated using an impulse response theory. In this case we convolve in time the rotational potential, which we denote by $\Lambda(\theta,\psi,t)$, with the relevant tidal viscoelastic Green's function.

$$R^{\mathrm{RN}}(\theta,\psi,t) = \Lambda(\theta,\psi,t) * \mathrm{GF}^{\mathrm{R,T}}(t), \tag{5}$$

and

$$\Phi^{\mathrm{RN}}(\theta,\psi,t) = \Lambda(\theta,\psi,t) * \mathrm{GF}^{\Phi,\mathrm{T}}(t), \tag{6}$$

where $R^{\mathrm{RN}}(\theta,\psi,t)$ and $\Phi^{\mathrm{RN}}(\theta,\psi,t)$ are the rotation-induced (hence the superscript RN) deformation of the radial position of the solid surface and the perturbation to the geopotential, respectively. The superscript T associated with the Green's functions denotes forcings associated with tidal (action at a distance) deformations of the planet. Expressions relating the rotational potential to perturbations in the rotation vector are given in Lambeck (1980) and Milne and Mitrovica (1996, 1998a). Furthermore, standard theories for computing GIA-induced variations in Earth rotation are provided, for example, by Sabadini et al. (1982) and Wu and Peltier (1984).

The total GIA-induced perturbations to the solid surface and the geopotential are therefore given by

$$R(\theta,\psi,t) = R^{\mathrm{L}}(\theta,\psi,t) + R^{\mathrm{RN}}(\theta,\psi,t) \tag{7}$$

and

$$\Phi(\theta,\psi,t) = \Phi^{\mathrm{L}}(\theta,\psi,t) + \Phi^{\mathrm{RN}}(\theta,\psi,t). \tag{8}$$

From (8), it follows that the GIA-induced height shift of the geoid is given by

$$\begin{aligned} G(\theta,\psi,t) &= \frac{1}{g}\left[\Phi^{\mathrm{L}}(\theta,\psi,t) + \Phi^{\mathrm{RN}}(\theta,\psi,t) + \Delta\Phi(t)\right] \\ &= G^{\mathrm{L}}(\theta,\psi,t) + G^{\mathrm{RN}}(\theta,\psi,t) + G^{\mathrm{SU}}(\theta,\psi,t) \\ &= G^{\mathrm{SV}}(\theta,\psi,t) + G^{\mathrm{SU}}(t). \end{aligned} \tag{9}$$

We have adopted in (9) the relation, $G^{\mathrm{SV}}(\theta,\psi,t) = G^{\mathrm{L}}(\theta,\psi,t) + G^{\mathrm{RN}}(\theta,\psi,t)$ to separate the spatially varying ('SV') and spatially uniform ('SU') components of the geoid change.

The uniform geoid shift $G^{\mathrm{SU}}(t)$ is computed by evoking conservation of surface ice–water mass. In a closed hydrological system, any mass lost (gained) by the ice sheets is gained (lost) by the oceans. Accordingly, the following simple relationship holds:

$$V_{\mathrm{OW}}(t) = -\frac{\rho_i}{\rho_w} V_{\mathrm{I}}(t), \tag{10}$$

where $V_{\mathrm{I}}(t)$ and $V_{\mathrm{ow}}(t)$ are the volumes of grounded ice and ocean water relative to the associated volume at the zero reference time. To ensure surface mass conservation, the surface integral of the GIA-induced sea-level change, $S(\theta,\psi,t)$, must equal V_{OW} at any time. That is

$$\left\langle G^{\mathrm{SV}}(\theta,\psi,t) - R(\theta,\psi,t)\right\rangle + G^{\mathrm{SU}}(t)A = V_{\mathrm{OW}}(t), \tag{11}$$

where A is the area of the oceans, and the brackets $\langle\ \rangle$ denote integration over the oceans. The first term in (11) gives the change in volume bounded by the original equipotential, (which coincided with the geoid at the reference time) and the surface of the ocean floor produced by load- and rotation-induced deformation. We can re-arrange the conservation of mass relation (11) to give $G^{\mathrm{SU}}(t)$ directly,

$$\begin{aligned} G^{\mathrm{SU}}(t) = \frac{V_{\mathrm{OW}}(t)}{A} - \frac{V_{\mathrm{DEF}}(t)}{A} &= -\frac{\rho_i}{\rho w}\frac{V_{\mathrm{I}}(t)}{A} \\ &\quad - \frac{\left\langle G^{\mathrm{SV}}(\theta,\psi,t) - R(\theta,\psi,t)\right\rangle}{A} \end{aligned} \tag{12}$$

in which we have adopted the notation $V_{DEF}(t)$ to represent the bracketed term in Eq. (11).

The appearance of $G^{\mathrm{SU}}(t)$ in Eq. (9) ensures that the change in the volume bounded by the upper and lower ocean surfaces is consistent with the change in the volume of ocean water.

The first term on the right-hand side in (12) has commonly been called the 'eustatic sea-level change' (e.g., Farrell and Clark, 1976; Mitrovica and Peltier, 1991; Peltier, 1994) which is the spatially uniform sea-level signal produced by direct mass exchange between the ice sheets and the oceans. Inconsistent use of this term within the GIA literature (e.g., Lambeck et al., 2001) has caused some confusion. In the following, we adhere to the conventional meaning and use the term 'eustatic' synonymously with 'meltwater'. The second term in (12), produced by load- and rotation-induced deformations of the geopotential and the solid surface, also contributes a significant spatially uniform sea-level signal that is crucial to properly understand and interpret far-field sea-level change (e.g., Clark et al., 1978; Mitrovica and Peltier, 1991) (see next section).

In recent work (Milne, 1998; Milne et al., 1999) we have emphasized that the sea-level equation (1) fails to

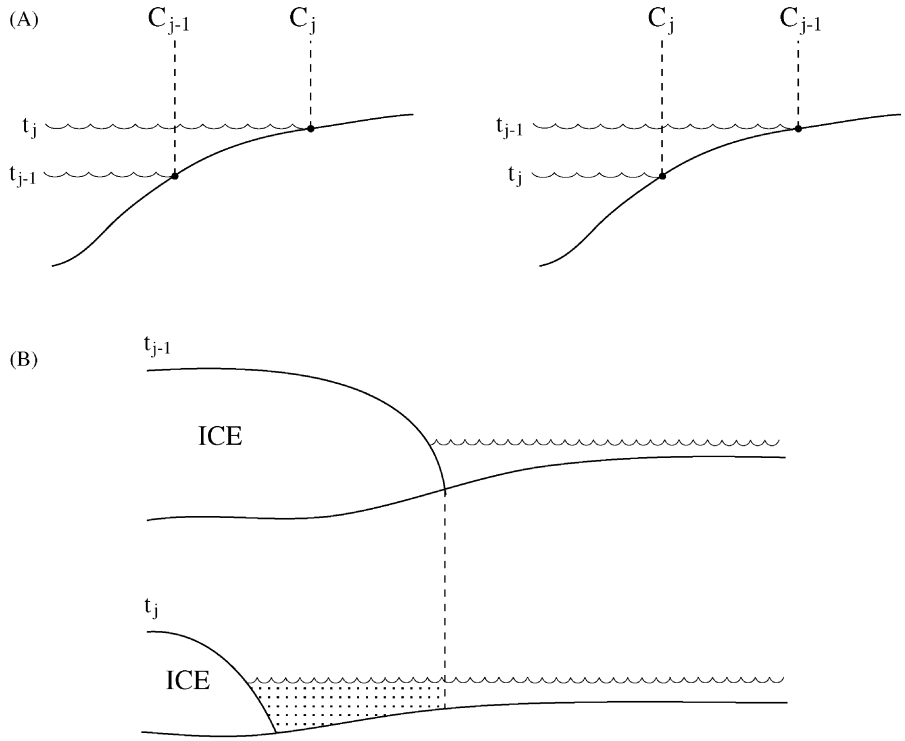

Fig. 1. Schematic diagrams illustrating processes influencing sea-level change that are not incorporated in the traditional (e.g., Farrell and Clark, 1976) sea-level theory (Eq. (1)). (A) Sea-level rise (left) and fall (right) and a time-varying shoreline geometry. (B) Sea-level change when a grounded marine ice sheet retreats. In this case, the sea-level change in the region vacated by ice is the total height difference between the geoid and the ocean floor rather than the difference between the GIA-induced perturbation to these surfaces.

account for two important GIA-related processes. The first is a time-dependence in the ocean function arising from the on-lap and off-lap of water on continental margins as sea level changes. This process is shown schematically in Fig. 1A and it has been treated in a number of recent studies (e.g., Lambeck and Nakada, 1990; Johnston, 1993; Peltier, 1994; Milne and Mitrovica, 1998b). The second involves the influx of water to sub-geoidal regions that are ice covered and subsequently exposed by a retreating ice margin (Fig. 1B). In such areas, during ice retreat, the sea-level change is not given by the GIA-induced *perturbations* to the geoid and the solid surface, but rather by the *absolute* height between the geoid and solid surface (see Fig. 1B). Milne (1998) and Milne et al. (1999) have used the terms 'water dumping' and 'water influx' to describe this process. Peltier (1998) later discussed a similar correction using the term 'implicit ice'.

Let us denote the change in sea-level during two successive time increments t_{j-1} and t_j by $\delta S(\theta,\psi,t_j)$. The sea-level change at the general time t_N is then given by

$$S(\theta,\psi,t_N)=\sum_{j=1}^{N}\delta S\big(\theta,\psi,t_j\big). \tag{13}$$

Following Milne (1998) and Milne et al. (1999), an extension of Eq. (1) that incorporates the two processes described in the preceding paragraph is

$$\begin{aligned}\delta S\big(\theta,\psi,t_j\big)=C\big(\theta,\psi,t_j\big)\big[\zeta\big(\theta,\psi,t_j\big)\big(&G^{\mathrm{SV}}\big(\theta,\psi,t_j\big)\\&+G^{\mathrm{SU}}\big(t_j\big)-R\big(\theta,\psi,t_j\big)-G^{\mathrm{SV}}\big(\theta,\psi,t_{j-1}\big)\\&-G^{\mathrm{SU}}\big(t_{j-1}\big)+R\big(\theta,\psi,t_{j-1}\big)\big)\\&+\big(\zeta\big(\theta,\psi,t_j\big)-1\big)T\big(\theta,\psi,t_j\big)\big].\end{aligned} \tag{14}$$

where the function $\zeta(\theta,\psi,t)$ takes the value zero in regions characterized by the retreat of grounded ice between t_{j-1} and t_j and the value of unity elsewhere (in practice, this field is defined by the adopted ice model). Furthermore, the definition of the ocean function, c, is extended so that it is zero in continental regions and in regions covered by grounded ice. The field $T(\theta,\psi,t)$ is the topography, that is, height of the solid surface relative to the geoid (details of how this field can be computed are given, for example, in Milne et al., 1999).

The sea-level described by (14) gives the same result as an incremental change based on (1) except at continental margins experiencing marine transgression or regression and in localized areas traversed by a retreating marine-based ice margin during times of ice retreat. For the latter case, $\zeta(\theta,\psi,t)$ is zero and (14) reduces to

$$\delta S\big(\theta,\psi,t_j\big)=-C\big(\theta,\psi,t_j\big)T\big(\theta,\psi,t_j\big) \tag{15}$$

and the sea-level change is given by the negative of the bathymetry. Thus, Eq. (14) predicts a relatively large

and positive sea-level change (and thus water load) in near-field regions that were vacated by a marine-based ice sheet at the time of ice retreat (see Fig. 1B). In contrast, the original equation (1) predicts a negative sea-level change in regions of marine-based ice retreat due, largely, to the solid-surface uplift and the reduced direct gravitational attraction of the ice sheet. As discussed in detail in Milne (1998), this represents an error of several hundreds of meters of water in some regions (e.g., Hudson Bay) and it has implications for previous estimates of both ice thickness and mantle rheology. As we discuss in the next section, predictions of far-field sea-level changes based on Eq. (14) are also markedly different from those based in Eq. (1). Put simply, the influx of water into ocean areas vacated by retreating ice will affect ocean levels even at great distances from the previously glaciated region.

The influence of near-field water influx on far-field sea level is evident when a revised version of Eq. (12) is written that includes the extensions inherent to Eq. (14),

$$\delta G^{\mathrm{SU}}(t_j) = \frac{\delta V_{\mathrm{OW}}(t_j)}{A_j} - \frac{\delta V_{\mathrm{DEF}}(t_j)}{A_j} - \frac{\delta V_{\mathrm{WI}}(t_j)}{A_j} = \delta G^{\mathrm{SU}}_{\mathrm{OW}}(t_j) + \delta G^{\mathrm{SU}}_{\mathrm{DEF}} + \delta G^{\mathrm{SU}}_{\mathrm{WI}}. \quad (16)$$

where (as in Eq. (13)) the symbol δ denotes a change from time $t = t_{j-1}$ to $t = t_j$ and so $G^{\mathrm{SU}}(t_N) = \sum_{j=1}^{N} \delta G^{\mathrm{SU}}(t_j)$; A_j is the area of the ocean basin at the time t_j, and $\delta V_{\mathrm{WI}}(t_j)$ is the volume of the ocean basin exposed by the retreating marine-based ice, which is given by

$$\delta V_{\mathrm{WI}}(t_j) = \left\langle \left(\zeta(\theta,\psi,t_j) - 1\right) T(\theta,\psi,t_j) \right\rangle_j, \quad (17)$$

where the symbol $\langle\,\rangle_j$ denotes integration over the ocean as it is predicted to exist at $t = t_j$. For the revised formalism (14), $\delta V_{\mathrm{DEF}}(t)$ is now given by

$$\delta V_{\mathrm{DEF}}(t_j) = \langle \zeta(\theta,\psi,t_j) \left(G^{\mathrm{SV}}(\theta,\psi,t_j) - R(\theta,\psi,t_j) - G^{\mathrm{SV}}(\theta,\psi,t_{j-1}) + R(\theta,\psi,t_{j-1})\right) \rangle_j \quad (18)$$

The third term in Eq. (16) gives the contribution of near-field water influx to the spatially uniform component of GIA-induced sea-level change. This term contributes $\sim 10\%$ to the total spatially uniform signal given by (16) (Milne et al., 1999; see next section) and thus it significantly affects predictions of far-field sea-level change even though the water influx mechanism occurs in near-field regions.

2.2. Far-field sea-level predictions

In this section we present a series of model predictions to illustrate the relative magnitudes of the various GIA-induced sea-level contributions discussed above. We adopt a pseudo-spectral algorithm (Mitrovica and Peltier, 1991; Milne, 1998) to solve the sea-level equation (14). To begin, we specify appropriate models for the rheology of the solid earth and the space–time history of the Late Pleistocene ice cover.

All predictions are based on Maxwell viscoelastic earth models that are spherically symmetric (i.e., parameters vary with radius only). The elastic and density structure of the model is based on the seismic model PREM (Dziewonski and Anderson, 1981). PREM has a radial discretization of 25 km in the mantle and 10 km in the crust. The non-elastic component of the rheology is more crudely parameterized into three layers. The Earth's lithosphere is modeled as an effectively elastic layer over GIA timescales by adopting a very high value of viscosity in an outer shell of prescribed thickness. A viscoelastic mantle region extends from the base of the model lithosphere to the core-mantle boundary (a depth of ~ 2900 km). This mantle region is separated in our models into two isoviscous layers termed the upper mantle (which extends to a depth of 670 km) and lower mantle (from 670 to 2900 km).

We adopt the ICE-3G deglaciation model (Tushingham and Peltier, 1991) as our initial input ice history. A glaciation phase is added to this model by assuming the same space–time variation (but reversed) during glaciation, and increasing the time increments between loading episodes from 1 to 7 cal. ka. The chronology for the original ICE-3G deglaciation history is based on the radiocarbon to calendar time scaling presented in Stuiver et al. (1986) (M. Tushingham, personal communication, 2000). We have revised the chronology to be consistent with the results of Bard et al. (1990).

We initially focus on Barbados (13.2°N, 59.5°W) because data from this location provided the first complete record of sea-level rise from the LGM through to the early Holocene (Fairbanks, 1989; Bard et al., 1990) and, as a consequence, have been employed to infer, either directly or via GIA modeling, the volume of glacial meltwater input to the ocean during the previous deglaciation (e.g., Peltier, 1994; Flemming et al., 1998). The dashed line in Fig. 2 is a solution to the traditional sea-level equation (1), revised to include a time-dependent continent margin, using the viscoelastic earth model adopted to construct the ICE-3G deglaciation history from a global distribution of near-field sea-level observations (Tushingham and Peltier, 1991). This earth model is comprised of a 120 km thick elastic lithosphere, an upper mantle viscosity of 10^{21} Pa s, and a lower mantle viscosity of 2×10^{21} Pa s. The total sea-level rise is ~ 115 m, of which ~ 108 m is due to the eustatic meltwater influx (corresponding to an excess LGM ice volume of $\sim 41 \times 10^6$ km^3). The ICE-3G model was not tuned to fit any far-field observations and so it is not surprising that the fit to the Barbados data is not particularly good. Tushingham and Peltier (1991) compared the magnitude of the meltwater rise predicted in Barbados to the observations of Bard et al. (1990) and

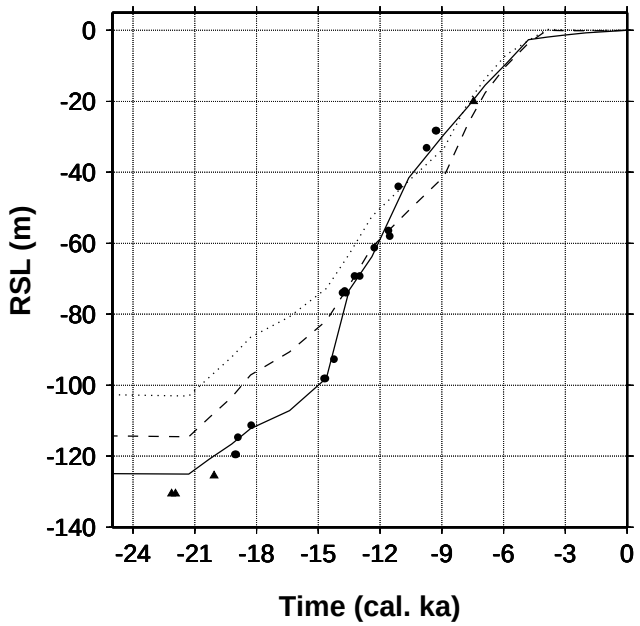

Fig. 2. The solid, dashed and dotted lines show sea-level predictions at Barbados (13.2°N, 59.5°W) based on three different GIA models (see main text). The dots and triangles are sea-level observations based on the coral species *Acropora palmata* (circles) and *Porites asteroides* (triangles) that have been corrected for tectonic uplift (Fairbanks, 1989; Bard et al., 1990).

noted that their model underestimated the data by about 5–10% (see discussion on their p. 4507).

As described in the last section, the traditional sea-level equation (1) does not incorporate the influence of near-field water influx into regions vacated by retreating ice. Indeed, the far-field sea-level rise predicted by the sea-level equation (1) will therefore be an overestimate of the correct sea-level rise for a given ice–earth model pairing. To illustrate this point, the dotted line in Fig. 2 is obtained by solving the revised sea-level equation (14) for the same ice–earth model pair used to calculate the dashed line. The total sea-level rise is predicted to be ~ 103 m in this case. The reduced sea-level rise, compared to the solution of Eq. (1), is predominantly due to meltwater (equivalent to ~ 9 m of sea-level) fluxing into the ocean basin volume exposed by retreating marine-based ice sheets (see Eqs. (16) and (17)). Most of the remaining discrepancy is due to the different water loading patterns in the two calculations. Therefore, an accurate sea-level prediction indicates that the ICE-3G deglaciation model contains an insufficient (by $\sim 20\%$) volume to fit the Barbados data. These results clearly demonstrate that an accurate inference of ice volume change since LGM requires the application of the near-field water influx mechanism incorporated in the revised sea-level theory (Eq. 14).

The ICE-3G model is outdated. It was constructed using an incorrect sea-level theory (Eq. 1) and an earth model which is not compatible with the results of a growing number of GIA modeling inferences. Recent work indicates that the average viscosity in the upper mantle is likely nearer to $3–5 \times 10^{20}$ Pa s than 10^{21} Pa s (e.g., Lambeck et al., 1990, 1998; Lambeck, 1993; Forte and Mitrovica, 1996; Mitrovica, 1996; Peltier, 1996; Wieczerkowski et al., 1999). Furthermore, estimates of the lower mantle viscosity currently lie within the range $5–50 \times 10^{21}$ Pa s (e.g., Nakada and Lambeck, 1989; Forte and Mitrovica, 1996; Mitrovica and Forte, 1997; Lambeck et al., 1998). Finally, inferences of lithospheric thickness vary widely (e.g., Fjeldskaar, 1994; Lambeck et al., 1998; Milne et al., 2001) although a value of 100 km is relatively representative.

Our goal in this article is not to argue for a specific ice or earth model, but rather to assess the various contributions to GIA-induced far-field sea-level rise. Accordingly, we follow a rather crude exercise to generate a 'standard' ice model that is tuned to roughly fit the Barbados sea-level data. First, we scale up the volume of the ICE-3G model by 20% (i.e., we increase the excess ice thickness at all geographic locations by 20%) to establish an approximate fit to the Barbados data (we can call this model ICE-3G2). Next, using an earth model constrained to be close to recently preferred values (an upper mantle viscosity of 5×10^{20} Pa s, a lower mantle viscosity of 10^{22} Pa s, and a lithospheric thickness of 100 km), we solve the new sea-level Eq. (14) using a sequence of ice models which have been iteratively modified from ICE-3G2 until a reasonably good fit to the Barbados data is obtained. This modification involved changing the amplitude of the ICE-3G2 load increments. The result of this exercise is shown by the solid line in Fig. 2. The total predicted sea-level rise from LGM to present should be interpreted as near the maximum that is consistent with this data set since the lowest three data points in Fig. 2 (triangles) correspond to the coral species *Porites asteroides*, which can live up ~ 20 m below the ocean surface.

Fig. 3 illustrates the form and magnitude of the GIA signals that contribute to the total prediction at Barbados. The solid line in Fig. 3 is the same as that in Fig. 2 and it shows the total predicted sea-level change at Barbados. This prediction is decomposed into the three remaining curves on the figure. The dashed line is the contribution to the spatially uniform sea-level change $G^{SU}(t)$ associated with meltwater addition, $\delta G^{SU}_{OW}(t)$ in Eq. (16). The dotted line is the contribution to the spatially uniform sea-level change arising from load- and rotation-induced deflections of the geoid and the ocean floor as well as the retreat of marine-based ice sheets (i.e., the remaining two terms in Eq. 16). The former contribution to the dotted line, which comprises approximately two-thirds of the total signal, is primarily due to ice-load-induced subsidence of the ocean floor in regions peripheral to centers of deglaciation as well as ocean-load-induced subsidence along continental

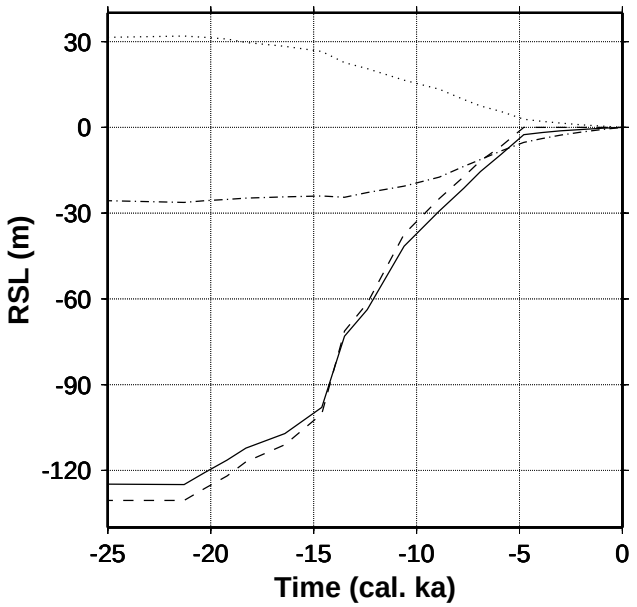

Fig. 3. The total predicted sea-level curve at Barbados (13.2°N, 59.5°W) (solid line) as well as a decomposition into three component parts. These components include the contributions to the spatially uniform sea-level change associated with meltwater addition (dashed line—$\delta G^{SU}_{OW}(t_j)$ in Eq. (16)), GIA-induced perturbations of the geopotential and the solid surface, and near-field water influx (dotted line—$\delta G^{SU}_{DEF}(t_j)$ and $\delta G^{SU}_{WI}(t_j)$ in Eq. (16)) respectively as well as the local (spatially variable) signal associated with ice-, ocean- and rotation-induced sea-level perturbations (dashed-dotted line).

margins (Mitrovica and Peltier, 1991; Mitrovica and Milne, 2001). Finally, the dashed-dotted line shows the spatially variable sea-level signal due to GIA (i.e., the right-hand-side of Eq. (14) with the spatially uniform term removed).

On inspection of Fig. 3, it is evident that the eustatic, or meltwater, contribution δG^{SU}_{OW} is the dominant contributor to the total signal. This is an expected result. However, the contributions from other sources discussed above are clearly an important part of the total sea-level response at this site. Indeed, these terms sum to produce the difference between the total predicted sea-level trend at Barbados (solid line) and the eustatic signal (dashed line). The inference of meltwater volumes based on observed sea-level records at far-field sites relies on the accuracy to which the non-meltwater signal (i.e., the difference between the solid and dashed lines) can be predicted.

To illustrate the spatial variability of the predicted sea-level signal we plot, in Fig. 4, relative sea-level predictions at four key far-field sites: Barbados (13.2°N, 59.5°W) (Fairbanks 1989; Bard et al., 1990), Bonaparte Gulf (12.0°S, 128.0°E) (Yokoyama et al., 2000), Huon Peninsula (6.0°S, 147.5°E) (Chappell and Polach 1991; Edwards et al., 1993), and Tahiti (18.0°S, 149.5°W) (Bard et al., 1996). Superimposed on each frame is the eustatic signal $\delta G^{SU}_{OW}(t)$ (which is, by definition, independent of location). At LGM the discrepancy (the meltwater curve minus total prediction) between the two curves on each frame varies from ~ -14 m (Huon Peninsula and Bonaparte Gulf) to ~ 2 m (Tahiti).

The site-dependence evident in Fig. 4 is a reflection of the distinct geographic sampling of the spatially variable GIA-induced sea-level signal (e.g., the dashed-dotted line in Fig. 3 for Barbados). To better understand the origin of this site-dependence we shall now explore this 'spatially variable' signal in more detail. As discussed in Section 2.1, the spatial variation has contributions from the ice and ocean components of the surface load as well as the GIA-induced perturbation to the rotational potential. These individual contributions are shown in Fig. 5A for each of the four far-field locations considered above.

The contributions of the ice-, ocean- and rotation-induced perturbations to the spatially varying component of the sea-level change at the four sites shows that the largest spatial variation results from the ocean loading. Compare, for example, the dotted lines for Bonaparte Gulf and Tahiti. Tahiti exhibits a rise in sea-level of ~ 12 m during deglaciation due to ocean loading. This rise is largely caused by the subsidence of the ocean floor around Tahiti in response to the loading of the south Pacific during deglaciation (e.g., Chappell, 1974). In contrast, the relatively small magnitude and more complex form of the ocean-load-induced signal at Bonaparte Gulf is a consequence of the considerable spatial migration of the coastline in this region, shown in Fig. 6. The late flooding of this area results in a much reduced and delayed ocean loading (e.g., Milne and Mitrovica, 1998b). The ocean-load-induced signal at Huon Peninsula is also distinct from the sea-level rise shown for Tahiti and Barbados and is due to the relatively complex coastal geometry in this area (see Fig. 6). These results illustrate the importance of incorporating a time-dependent ocean-continent geometry in the sea-level model (e.g., Lambeck and Nakada 1990; Johnston, 1993; Peltier, 1994).

The ice-induced component of the spatially varying sea-level signal is remarkably similar at each of the sites, especially those in the southern hemisphere. Additional calculations (not shown here) indicate that the signal for the sites located in the southern hemisphere is dominated by the direct gravitational attraction of the ice model. Northern hemisphere ice accounts for almost 80% of the total excess ice volume in our standard ice model at the LGM. The redistribution of this ice mass into the ocean basins during deglaciation produces a geoid drop in regions surrounding the ancient ice centers compared to a geoid rise in far-field regions (e.g., Woodward, 1888). The ice-load-induced signal at Barbados, although similar to that at the three southern hemisphere sites, is not dominated by the direct effect of the wasting ice masses. Note that the total sea-level rise

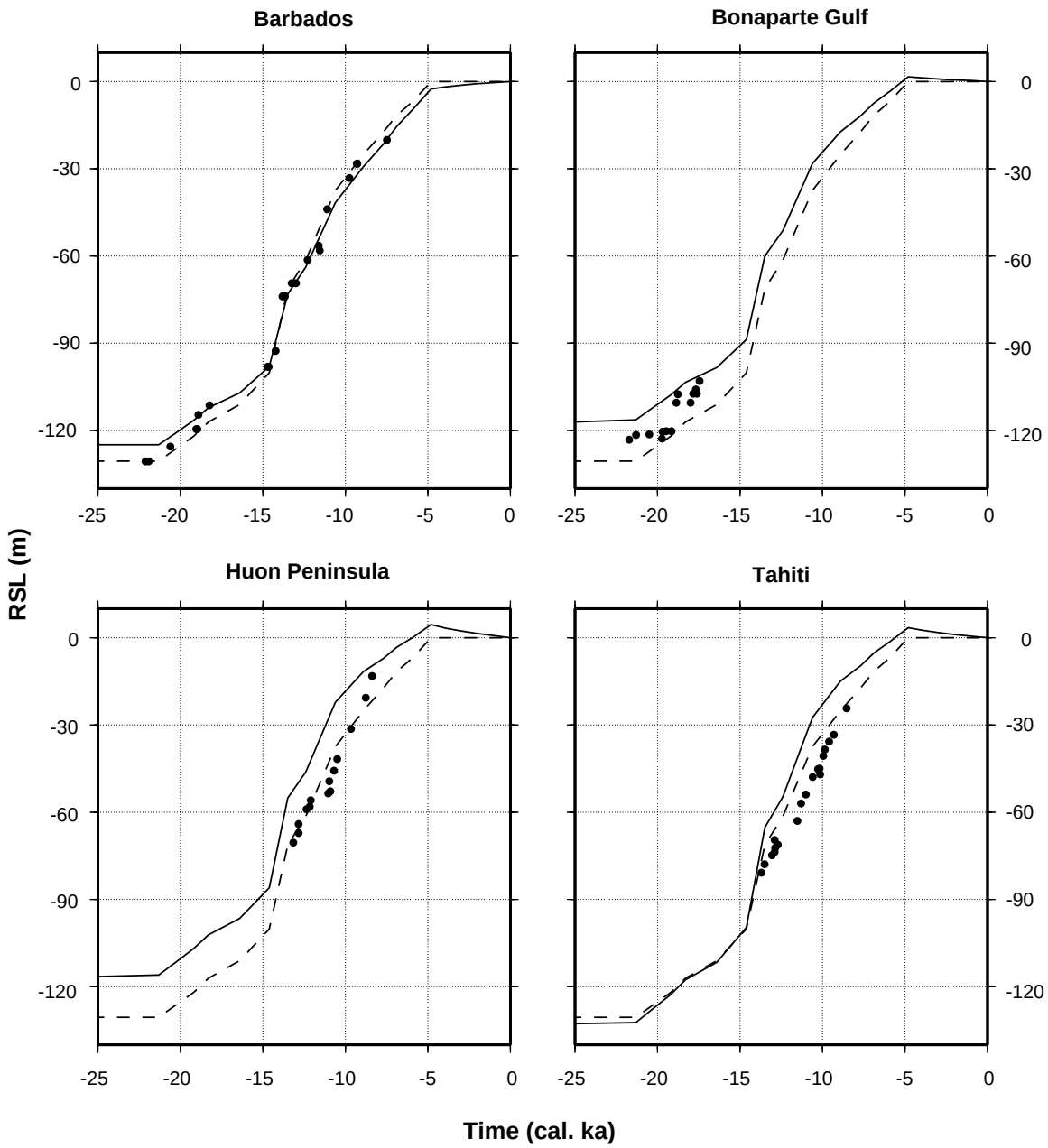

Fig. 4. Solid lines show sea-level predictions based on our standard GIA model (see text) at Barbados (13.2°N, 59.5°W), Bonaparte Gulf (12.0°S, 128.0°E), Huon Peninsula (6.0°S, 147.5°E), and Tahiti (18.0°S, 149.5°W). Dashed lines show contribution of meltwater volume to the spatially uniform sea-level signal, $\delta G^{SU}_{OW}(t_j)$, in Eq. (16). The dots superimposed on the curves represent observational constraints.

at this site (compared to the southern hemisphere sites) is smaller in magnitude and the predicted rise is smoother and less rapid. These differences arise from the relative proximity of this site to the Laurentide ice sheet. The ice-induced sea-level rise at Barbados is dominated by the solid-surface subsidence in this area.

The rotation-induced signal shows a non-monotonic temporal evolution at all four sites. The origin of this non-monotonicity has been discussed in detail in Milne and Mitrovica (1998a). The rotation-induced signal has a spatial dependence described by a degree two and order one spherical harmonic function that resembles a four-quadrant beachball (e.g., Han and Wahr, 1989; Milne and Mitrovica, 1998a). Accordingly, antipodal sites (Barbados versus Bonaparte Gulf or Huon Peninsula) will show the same trends, while sites in the remaining quadrants of the so-called 2–1 geometry (e.g., Tahiti) will have trends that are reversed in sign. The rotation signal is of relatively small amplitude ($\leqslant 3$ m) because these sites are all relatively close to the equator

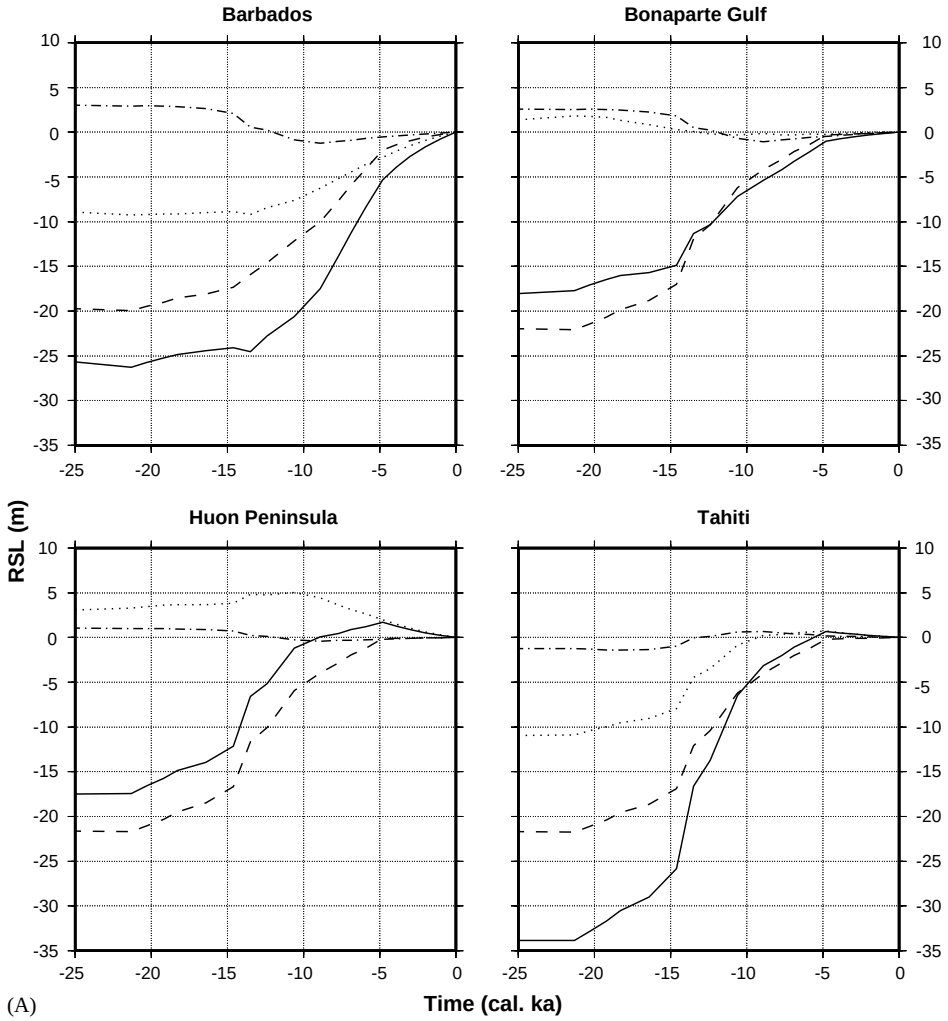

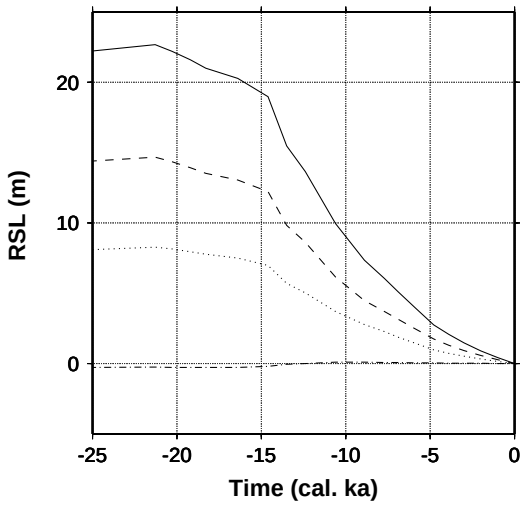

Fig. 5. (A) Plots of the spatially varying sea-level signal produced by perturbations to the geopotential and the solid surface from the surface load and rotational potential (solid lines). Decomposition of this signal into contributions associated with ice loading (dashed line), ocean loading (dotted line) and rotation-induced effects (dashed-dotted line) is illustrated. Results are shown for the four sites considered in Fig. 4. (B) The spatially uniform component of the sea-level signal associated with the ice-load-induced (dashed line), ocean-load-induced (dotted line) and rotation-induced (dashed-dotted line) perturbations to the geopotential and the solid surface. The spatially uniform signal associated with the net signal (solid line in Fig. 5A) is shown by the solid line.

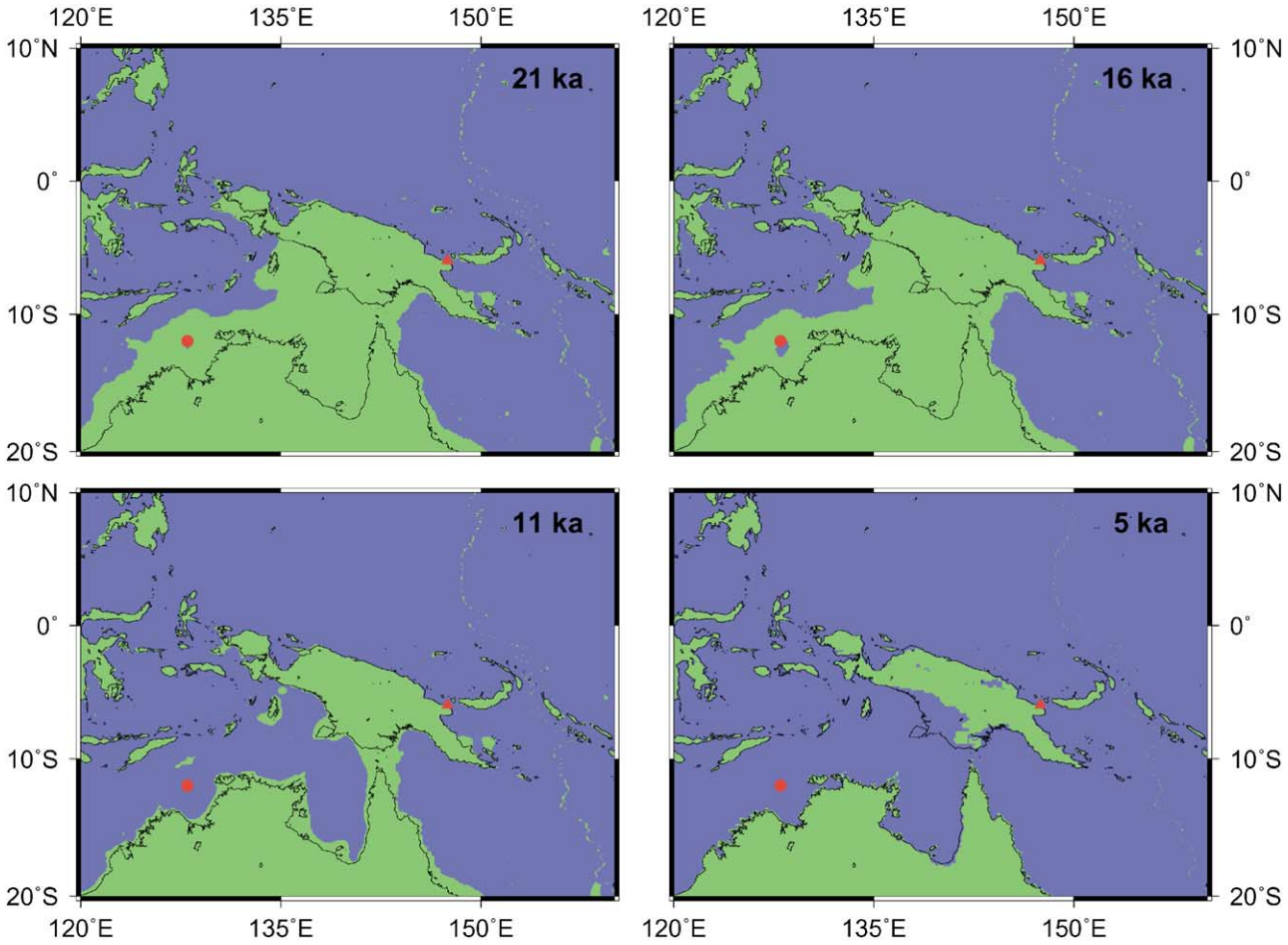

Fig. 6. Predictions of the coastline geometry in northern Australia and Papua New Guinea at four distinct times extending from the last glacial maximum to the end of our model deglaciation event at 5 cal. ka BP (all times shown represent the calendar time scale). The locations of Bonaparte Gulf and Huon Peninsula sea-level observations are given by the small red dot and triangle, respectively.

(a great circle node in the 2–1 geometry). Nevertheless, site-to-site differences can reach 5 m, and these differences account for a non-negligible portion of the site variation evident in Fig. 4. As an example, the rotation signal accounts for approximately one-third of the total difference in predicted sea level at LGM between Tahiti and Bonaparte Gulf.

The predictions shown in Fig. 5A provide useful insight to the origin of the spatial variation in the predicted RSL signals shown in Fig. 4. However, it is important to note that the sea-level curves shown in Fig. 5A do not represent the *total* ice-, ocean- and rotation-induced components of sea-level change. The total signal associated with each of these GIA forcings is the sum of their respective spatially varying component (shown by the dashed, dotted and dash-dotted lines in Fig. 5A) with a spatially uniform term associated with the geopotential and solid surface deformation integrated over the ocean area (i.e., the contribution of either the ice-, ocean or rotation-induced signal to the right-hand side of Eq. (18)). For this reason, the relative magnitudes of the total sea-level contributions from the ice and ocean loading and the rotational potential may not be accurately represented in Fig. 5A. The spatially uniform signals associated with each of the GIA-forcings considered in Fig. 5A are shown in Fig. 5B.

The deformation of the solid surface and the geopotential produced by the ice and ocean loading both contribute to a significant geoid fall from the LGM to the present (Mitrovica and Peltier 1991; Mitrovica and Milne 2001). Therefore, the spatially uniform component of these signals will, in general, act to reduce the total magnitude of the predicted ice- and ocean-induced signals at the four sites. (Note, however, that the net ocean-induced signal is amplified at Huon Peninsula and Bonaparte Gulf since the local ocean loading at this site produces a sea-level fall during deglaciation; see Fig. 5A). The rotation-induced signal, in contrast, produces a relatively small spatially uniform signal and so the results in Fig. 5A can be treated as a relatively accurate representation of the total rotation-induced signal.

We next consider the sensitivity of the predicted sea-level signals at Barbados to variations in the viscosity parameterization of the earth model. A series of calculations were performed in which the lithospheric thickness, upper mantle and lower mantle viscosity were varied over plausible ranges. Our predictions showed no significant variation for lithospheric thicknesses ranging from 70 to 120 km and so these results will not be considered further. In Fig. 7 we explore the sensitivity of the decomposition performed in Fig. 3 to variations in the upper and lower mantle viscosity. The top plot shows predictions of the sea-level components for earth models that are identical to the standard model except that the upper mantle viscosity is reduced to 2×10^{20} Pa s (red lines) or increased to 10^{21} Pa s (blue lines). The bottom plot shows predictions in which the lower mantle viscosity is reduced to 5×10^{21} Pa s (red lines) or increased to 5×10^{22} Pa s (blue lines).

The total sea-level rise predicted for the stronger upper mantle model is just over 5 m larger than than the prediction for the weaker upper mantle case. Note that this variation is caused, largely, by a perturbation to the spatially uniform signal (dotted line) and so will impact all locations. The curves diverge by a similar amount in the early Holocene due, in this case, to local loading and rotational effects (dash-dotted lines). Varying the viscosity of the lower mantle produces a larger change in the total sea-level rise predicted at Barbados. The net effect reaches ~ 18 m at LGM and it decreases almost monotonically from LGM to the present. Note that the magnitudes of the non-meltwater contribution to the spatially uniform sea-level change (dotted lines) and the spatially variable GIA signal (dashed-dotted lines) decrease with increased lower mantle viscosity. This is an expected trend since the rate of mantle flow will be progressively reduced as the deep mantle is stiffened. We conclude that uncertainties associated with mantle viscosity can be a limitation to the accuracy of sea-level predictions within the far-field. As we discuss in the next section, this uncertainty will, in turn, impact the accuracy to which meltwater volumes can be inferred from such data.

In the above analysis we have not addressed a number of potentially important uncertainties associated with the earth model adopted in the sea-level calculations. These include the impact of fine-scale, large amplitude changes in viscosity with depth (e.g., Milne et al., 1998), deviations in the rheology from a simple linear viscous flow law (e.g., Karato, 1998; Ranalli, 1998; Wu, 1999) and the undoubted presence of lateral variation in both elastic and viscous structure (e.g., Manga and O'Connell, 1995; Kaufmann et al., 1997). Also, note that the influence of changes in ocean water salinity and temperature on sea level are not incorporated in the model.

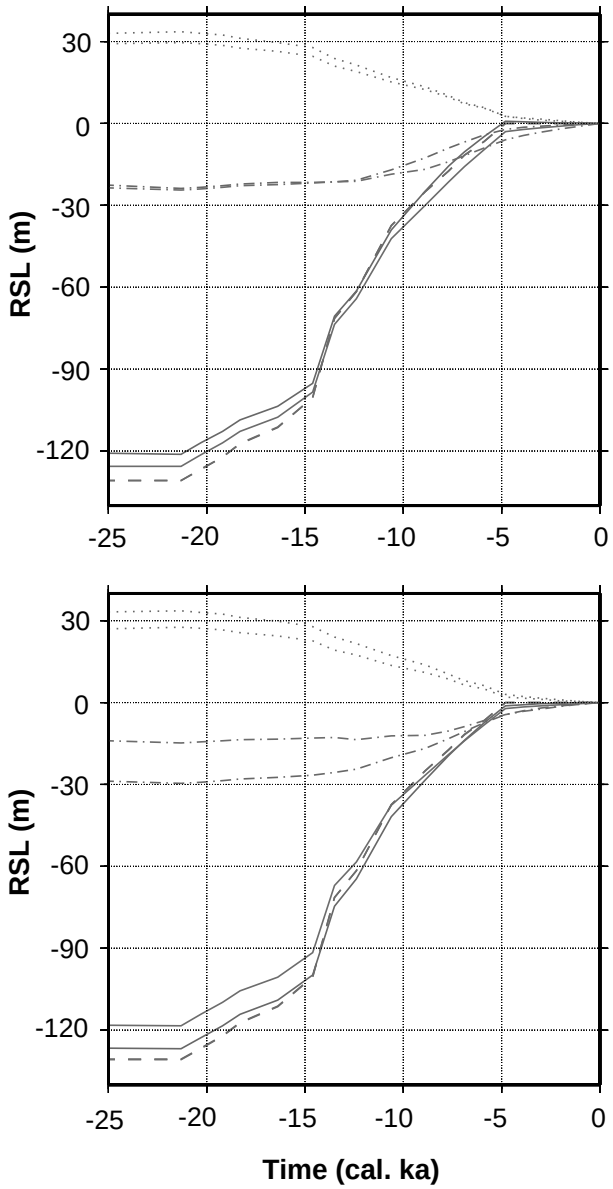

Fig. 7. Sea-level predictions at Barbados (13.2°N, 59.5°W) based on a suite of earth models. The format of each figure is the same as that adopted for Fig. 3. The lines in the top frame show predictions based on our standard model except that the upper mantle viscosity is changed to either 2×10^{20} Pa s or 10^{21} Pa s, respectively. The lines in the bottom show predictions based on our standard model except that the lower mantle viscosity is either 5×10^{21} Pa s or 5×10^{22} Pa s, respectively.

3. Inferring continental ice volume from far-field sea-level observations

As stated in the Introduction, observations of far-field sea-level rise provide the most direct estimate of the volume of grounded ice existing between the LGM and the present. In this section we build on the results presented above to review the principal ideas related to this inference procedure.

It will be useful in this discussion to rewrite Eq. (14) in the highly simplified form:

$$\delta S(\theta,\psi,t_j) = \delta S_{\mathrm{NMW}}(\theta,\psi,t_j) + C(\theta,\psi,t_j)\delta G^{\mathrm{SU}}_{\mathrm{OW}}(t_j). \quad (19)$$

Eq. (19) emphasizes that observed sea-level changes (the left-hand-side of the equation) differ from the meltwater contribution by a term that combines all the remaining effects of GIA.

Eq. (19) also serves as a useful basis to describe previous efforts to estimate ice volumes, $V_{\mathrm{I}}(t)$, which are directly linked to the meltwater contribution, $G^{\mathrm{SU}}_{\mathrm{OW}}(t)$, through Eqs. (10) and (16), from far-field sea-level observations. In general, the literature includes two rather distinct approaches to this problem. One method involves establishing a preferred ice-earth model pair (or a suite of preferred models) and using these models to predict the first term on the right-hand side of Eq. (19) for a particular site of interest. These predictions can then be used to correct the observed sea-level signal and thus estimate the eustatic sea-level change (following Eq. (19)). This procedure can be repeated for a group of far-field sites and a suitable average obtained (e.g., Flemming et al. (1998)). A second approach is evident, for example, in Peltier (1994). In this case an ice–earth model pair are established which provide an acceptable fit to the observed sea-level variation at a specific far-field site (e.g., Barbados in the case of Peltier, 1994). Ice volumes are then directly obtained from the input model. Ideally, the 'true' ice–earth model pair should provide a good fit to all far-field sea-level observations, and the two procedures would yield consistent results.

The effort to estimate ice volume changes since the LGM is clearly influenced by the accuracy of the adopted models of Late Pleistocene ice cover and the Earth's viscoelastic structure, as well as the accuracy of the sea-level theory (e.g., see Fig. 2) adopted to predict sea-level changes given these model inputs. In this regard, we note that previous estimates by the independent groups cited above have been based on distinct ice–earth model pairs and, perhaps, sea-level theories. In the remainder of this section we apply the results of the previous section to estimate ice volume changes since the LGM through the analysis of observations at Barbados and Bonaparte Gulf. (We note that data recently obtained from the Sunda Shelf (Hanebuth et al., 2000) can also be employed for this purpose. We hope to consider the constraints imposed by these data, alongside those derived from Barbados and Bonaparte Gulf data, in a future study.)

In Section 2.2 we adopted a specific earth model and tuned (that is, modified) the ICE-3G model until we obtained a good fit to the Barbados sea-level observations (solid line, Fig. 2). Thus, following the second methodology described above, our estimate of ice volume changes since the LGM are trivially given by the mass balance of the ice model. Our revised ICE-3G model has an excess ice volume of $49.5 \times 10^6\,\mathrm{km}^3$. This value maps into a total meltwater contribution to eustatic sea-level change, $G^{\mathrm{SU}}_{\mathrm{OW}}(t)$, or alternatively an 'ice-equivalent' sea-level change, of ~ 130 m. We note that our predicted sea-level curve for Barbados falls about 5 m above the oldest *Porites asteroides* data in the observational record. We have already noted that this coral species can live to depths of ~ 20 m below the ocean surface, and thus it is prudent to intercept this estimate of excess ice volume as near the maximum consistent with these observations.

Next, we turn to an estimate of ice volume changes based on predictions at a set of far-field sites (the first methodology described above). Specifically, we will consider sea-level observations at Barbados and Bonaparte Gulf. We choose the deepest LGM sea-level indicator at Barbados (the *Porites asteroides* datum at ~ 130 m below present sea level) so as to estimate a maximum LGM excess ice volume for these data based on our standard earth–ice model pair. From Fig. 4, our ice–earth model pairing indicates a discrepancy of 5 m between predicted sea level at LGM and the meltwater contribution to eustatic sea-level change. Accordingly, we estimate $G^{\mathrm{SU}}_{\mathrm{OW}} \sim 135$ m from this datum. If we adopt a different interpretation and assume that the coral on which this datum is based lived at a depth of 20 m below mean sea level, a significantly reduced meltwater sea-level contribution of ~ 115 m is obtained, which maps into an excess ice volume at the LGM of $43.5 \times 10^6\,\mathrm{km}^3$.

Yokoyama et al. (2000) have published sea-level data for Bonaparte Gulf, including a 21.3 cal. ka BP datum at 121.4 m below present mean sea-level. (During the EPILOG meeting, some discussion arose concerning the interpretation of the deepest sea-level indicators identified by Yokoyama et al. (2000). Until this issue is resolved, we shall adopt the interpretation put forward by Yokoyama et al. (2000).) From Fig. 4, our predictions at this site (and at this age) show a discrepancy of ~ -14 m between predicted sea level and $G^{\mathrm{SU}}_{\mathrm{OW}}$. Therefore, we estimate a meltwater or eustatic sea-level contribution of ~ 135 m from this datum, which is consistent with the maximum meltwater rise that can be inferred from the Barbados data (based on our predictions). This magnitude of sea-level rise is equivalent to an excess ice volume of $51 \times 10^6\,\mathrm{km}^3$ at the LGM. Note that, despite a difference of almost 9 m between the depths of the Barbados and Bonaparte Gulf data points considered above, our analysis reveals that they yield consistent LGM ice volume estimates if the Barbados datum considered is assumed to mark the height of the LGM ocean surface.

Our inferred meltwater contribution (or, equivalently, LGM ice volume) is consistent with the value estimated by Yokoyama et al. (2000) on the basis of data from Bonaparte Gulf. In addition, we note that our ice–earth model pair also provides a satisfactory fit to the

observed sea-level curve for Bonaparte Gulf. Our predicted sea-level at LGM (~ 117 m from Fig. 4) is reasonably close to the observational constraint cited by Yokoyama et al. (2000). We remind the reader that our ice–earth model pair was tuned to fit the Barbados data alone.

We can use the results in Fig. 7 to estimate the uncertainty in our estimate of ice volumes (or, alternatively, the meltwater contribution to sea-level change) arising from errors in the adopted radial earth model. The predicted sea-level change at Barbados since the LGM is 119 and 127 m for lower mantle viscosity values of 50×10^{21} Pa s and 5×10^{21} Pa s, respectively. These predictions result in LGM ice volume estimates (assuming that *the Porites asteroides* datum accurately represents the mean sea level at this time) of, respectively, 53×10^3 km^3 and 50×10^3 km^3. That is, a plausible range of lower mantle viscosity values maps into an uncertainty of roughly $\pm 1.5 \times 10^6$ km^3 in the LGM ice volume inference from Barbados data.

4. Summary

We have reviewed recent advances in the theoretical treatment of GIA-induced sea-level changes and have applied a recently revised theory to predict sea-level histories at four far-field sites (Barbados, Bonaparte Gulf, Huon Peninsula and Tahiti). The theoretical advances include the incorporation of both rotational effects on sea-level and a time-dependent shoreline geometry, as well as an accurate treatment of sea-level change in regions of ice retreat. Our application of the revised theory was based on a radial viscoelastic earth model that is representative of recent independent inferences from the literature, and an ice model modified from the ICE-3G deglaciation history in order to fit observational constraints at Barbados.

The overriding goal of the study was *not* to argue for the veracity of our standard ice-earth model pairing, but rather to use this pairing as a tool for elucidating the physics of far-field sea-level change associated with GIA. To this end, we de-constructed the total predicted sea-level variation into spatially uniform versus spatially varying signals and we isolated contributions from ice loading, ocean loading and rotational effects. This exercise was performed to satisfy three specific objectives: (1) to isolate the impact of the recent advances in sea-level theory on predictions of sea-level change at far-field sites, with special emphasis on the process of water influx into regions of ice retreat; (2) to explore in detail the discrepancy between the total predicted signal at these sites and the meltwater (or eustatic) contribution to sea-level change; (3) to critically review the methods used to estimate the deglaciation-induced meltwater flux (and thus past ice volumes) from far-field sea-level observations, and to apply these methods using the understanding developed in (1) and (2).

We have concluded that each of the improvements to the traditional sea-level theory of Farrell and Clark (1976) has an impact on predictions of far-field sea-level change. Water influx into regions vacated by a retreating marine-based ice margin introduces both a local (near-field) and spatially uniform component to the predicted sea-level change, and the latter (with an amplitude of ~ 10 m) impacts predictions at all far-field sites by roughly the same amount. The influence of rotational effects and a time-dependent ocean-continent interface are, in contrast, more spatially variable within the far-field. The rotation signal approaches zero toward the equator and can change sign as one passes from one quadrant to another within the degree two and order one geometry that characterizes this signal. The impact of a time-varying shoreline depends on the detailed ocean-continent geometry and bathymetry in the vicinity of a given site.

The meltwater contribution to far-field sea-level change dominates the predicted signal. Discrepancies between the meltwater curve, and the total predicted signal arise from a rather complicated sum of ice, ocean and rotation-induced deformations as well as spatially uniform effects associated, for example, with water influx in regions of ice retreat. For our adopted ice–earth model, the discrepancy at LGM (meltwater minus total signal) ranges from -14 m (Huon Peninsula, Bonaparte Gulf) to 2 m (Tahiti), although we have demonstrated that this discrepancy can be sensitive to viscosity variations in the radial viscoelastic earth model. The discrepancy is also time-dependent, reflecting the temporal evolution of the various GIA-related contributions.

The meltwater component of the far-field sea-level rise can be estimated by correcting the observations for the contributions from the remaining GIA-related effects. This 'correction' procedure has been explicitly performed in some recent studies by applying a sea level-to-meltwater mapping computed on the basis of a preferred ice–earth model pairing (e.g., Flemming et al., 1998; Yokoyama et al., 2000). The correction is implicit in studies where ice–earth model pairing are tuned to fit a specific far-field relative sea-level history (e.g., Peltier, 1994). In this case, the meltwater curve is taken directly from the ice model.

We have applied these various procedures to the observational record at Barbados and Bonaparte Gulf. We have obtained estimates of excess ice volumes at LGM ranging from 43.5×10^6 km^3 (equivalent to a meltwater contribution to eustatic sea-level rise of about 115 m), to 51×10^6 km^3 (a meltwater contribution of 135 m) based on two contrasting interpretations of Barbados coral data. We also obtained an ice volume estimate of 51×10^6 km^3 based on the more recent

Bonaparte Gulf data. This latter estimate is consistent with with an independent analysis of the Bonaparte Gulf data (Yokoyama et al., 2000).

A more robust estimate of eustatic sea-level change since the LGM requires that other far-field data (such as those from the Sunda Shelf) be brought to bear. However, the basic principles involved in mapping sea-level observations to an estimate of the eustatic or meltwater signal, described herein, remains valid.

Acknowledgements

We thank both Tom James and Pat Wu for constructive reviews. The research presented in this manuscript was partially funded by the Royal Society of the United Kingdom.

References

Bard, E., Hamelin, B., Fairbanks, R.G., Zindler, A., 1990. Calibration of the ^{14}C timescale over the past 30,000 years using mass spectrometric U–Th ages from Barbados corals. Nature 345, 405–410.

Bard, E., Hamelin, B., Arnold, M., Montaggioni, L., Cabioch, G., Faure, G., Rougerie, F., 1996. Deglacial sea-level record from Tahiti corals and the timing of global meltwater discharge. Nature 382, 241–244.

Bills, B.G., James, T.S., 1996. Late Quaternary variations in relative sea level due to glacial cycle polar wander. Geophysical Research Letters 23, 3023–3026.

Bloom, A.L., 1967. Pleistocene shorelines: a new test of isostasy. Geological Society of America Bulletin 78, 1477–1494.

Chappell, J., 1974. Late Quaternary glacio- and hydro-isostasy, on a layered earth. Quaternary Research 4, 429–440.

Chappell, J., Polach, H., 1991. Post-glacial sea-level rise from a coral record at Huon Peninsula, Papua New Guinea. Nature 349, 147–149.

Clark, J.A., Farrell, W.E., Peltier, W.R., 1978. Global changes in postglacial sea level: a numerical calculation. Quaternary Research 9, 265–287.

Daly, R.A., 1925. Pleistocene changes of level. American Journal of Science 10, 281–313.

Dziewonski, A.M., Anderson, D.L., 1981. Preliminary reference earth model (PREM). Physics of the Earth and Planetary Interions 25, 297–356.

Edwards, R.L., Beck, J.W., Burr, G.S., Donahue, D.J., Chappell, J.M.A., Bloom, A.L., Druffel, E.R.M., Taylor, F.W., 1993. A large drop in atmospheric $^{14}C/^{12}C$ and reduced melting in the younger dryas, documented with ^{230}Th ages of corals. Science 260, 962–968.

Fairbanks, R.G., 1989. A 17,000-year glacio-eustatic sea-level record: influence of glacial melting rates on the younger dryas event and deep-ocean circulation. Nature 342, 637–642.

Farrell, W.E., Clark, J.A., 1976. On postglacial sea level. Geophysical Journal of the Royal Astronomical Society 46, 647–667.

Fjeldskaar, W., 1994. Viscosity and thickness of the asthenosphere detected from the Fennoscandian uplift. Earth and Planetary Science Letters 126, 399–410.

Flemming, K., Johnston, P., Zwartz, D., Yokoyama, Y., Lambeck, K., Chappell, J., 1998. Refining the eustatic sea-level curve since the Last Glacial Maximum using far- and intermediate-field sites. Earth and Planetary Science Letters 163, 327–342.

Forte, A.M., Mitrovica, J.X., 1996. A new inference of mantle viscosity based on a joint inversion of post-glacial rebound data and long-wavelength geoid anomalies. Geophyscial Research Letters 23, 1147–1150.

Haskell, N.A., 1935. The motion of a viscous fluid under a surface load. Physics 6, 56–61.

Hanebuth, T., Stattegger, K., Grootes, P.M., 2000. Rapid flooding of the Sunda Shelf: a late-glacial sea-level record. Science 288, 1033–1035.

Han, D., Wahr, J., 1989. Post-glacial rebound analysis for a rotating Earth. In: Cohen, S., Vanicek, P. (Eds.), Slow Deformations and Transmission of Stress in the Earth. AGU Monograph Series 49, 1–6.

Jamieson, T.F., 1865. On the history of the last geological changes in Scotland. Quaternary Journal of the Geological Society of London 21, 161–203.

Johnston, P., 1993. The effect of spatially non-uniform water loads on predictions of sea level change. Geophysical Journal International 114, 615–634.

Karato, S., 1998. Micro-physics of post glacial rebound. In: Wu, P. (Ed.), Dynamics of the Ice Age Earth: A Modern Perspective. Trans Tech Publications Ltd., Switzerland, pp. 351–364.

Kaufmann, G., Wu, P., Wolf, D., 1997. Some effects of lateral heterogeneities in the upper mantle on postglacial land uplift close to continental margins. Geophysical Journal International 128, 175–187.

Lambeck, K., 1980. The Earth's Variable Rotation. Cambridge University Press, Cambridge, UK.

Lambeck, K., 1993. Glacial rebound of the British Isles-II. A high resolution, high-precision model. Geophysical Journal International 115, 960–990.

Lambeck, K., Johnston, P., Nakada, M., 1990. Holocene glacial rebound and sea-level change in NW Europe. Geophysical Journal International 103, 451–468.

Lambeck, K., Nakada, M., 1990. Late Pleistocene and Holocene Sea-level change along the Australian coast. Palaeogeog. Palaeoclimat. Palaeoecol. 89, 143–176.

Lambeck, K., Smither, C., Johnston, P., 1998. Sea-level change, glacial rebound and mantle viscosity for northern Europe. Geophysical Journal International 134, 102–144.

Lambeck, K., Yokoyama, Y., Johnston, P., Purcell, A., 2001. Corrigendum to "Global ice volumes at the Last Glacial Maximum and early Lateglacial". Earth and Planetary Science Letters 190, 275.

Manga, M., O'Connell, R.J., 1995. The tectosphere and postglacial rebound. Geophysical Research Letters 15, 1949–1952.

Milne, G.A., 1998. Refining models of the glacial isostatic adjustment process. Ph.D. thesis, University of Toronto, Toronto, Canada.

Milne, G.A., Mitrovica, J.X., 1996. Postglacial sea-level change on a rotating Earth: first results from a gravitationally self-consistent sea-level equation. Geophysical Journal International 126, F13–F20.

Milne, G.A., Mitrovica, J.X., 1998a. Postglacial sea-level change on a rotating Earth. Geophysical Journal International 133, 1–19.

Milne, G.A., Mitrovica, J.X., 1998b. The influence of a time-dependent ocean-continent geometry on predictions of post-glacial sea level change in Australia and New Zealand. Geophysical Research Letters 25, 793–796.

Milne, G.A., Mitrovica, J.X., Forte, A.M., 1998. The sensitivity of GIA predictions to a low viscosity layer at the base of the upper mantle. Earth and Planetary Science Letters 154, 265–278.

Milne, G.A., Mitrovica, J.X., Davis, J.L., 1999. Near-field hydro-isostasy: the implementation of a revised sea-level equation. Geophysical Journal International 139, 464–482.

Milne, G.A., Davis, J.L., Mitrovica, J.X., Scherneck, H.-G., Johansson, J.M., Vermeer, M., Koivula, H., 2001. Space-Geodetic

constraints on glacial isostatic adjustment in Fennoscandia. Science 291, 2381–2385.
Mitrovica, J.X., 1996. Haskell [1935] revisited. Journal of Geophysical Research 101, 555–569.
Mitrovica, J.X., Forte, A.M., 1997. The radial profile of mantle viscosity: results from the joint inversion of convection and post-glacial rebound observables. Journal of Geophysical Research 102, 2751–2769.
Mitrovica, J.X., Milne, G.A., 2001. On the origin of ocean syphoning. Geophysical Journal International submitted.
Mitrovica, J.X., Peltier, W.R., 1991. On post-glacial geoid subsidence over the equatorial oceans. Journal of Geophysical Research 96, 20053–20071.
Munk, W.H., MacDonald, G.J.F., 1960. The Rotation of the Earth. Cambridge University Press, Cambridge.
Nakada, M., Lambeck, K., 1987. Glacial rebound and relative sea-level variations: a new appraisal. Geophysical Journal of the Royal Astronomical Society 90, 171–224.
Nakada, M., Lambeck, K., 1989. Late Pleistocene and Holocene sea-level change in the Australian region and mantle rheology. Geophysical Journal International 96, 497–517.
Peltier, W.R., 1974. The impulse response of a Maxwell Earth. Reviews of Geophysics 12, 649–669.
Peltier, W.R., 1994. Ice age paleotopography. Science 265, 195–201.
Peltier, W.R., 1996. Mantle viscosity and ice-age ice sheet topography. Science 273, 1359–1364.
Peltier, W.R., 1998. 'Implicit ice' in the global theory of glacial isostatic adjustment. Geophysical Research Letters 25, 3955–3958.
Peltier, W.R., Andrews, J.T., 1976. Glacial isostatic adjustment—I. The forward problem. Geophysical Journal of the Royal Astronomical Society 46, 605–646.
Pirazolli, P.A., 1991. World Atlas of Holocene Sea-Level Changes. Elsevier Oceanography Series, Vol. 58.
Ranalli, G., 1998. Inferences on mantle rheology from creep laws. In: Wu, P. (Ed.), Dynamics of the Ice Age Earth: A Modern Perspective. Trans Tech Publications Ltd., Switzerland, pp. 323–340.
Sabadini, R., Yuen, D.A., Boschi, E., 1982. Polar wandering and the forced responses of a rotating, multilayered, viscoelastic planet. Journal of Geophysical Research 87, 2885–2903.
Shennan, I., Innes, J.B., Long, A.J., Zong, Y., 1995. Late Devensian and Holocene relative sea-level changes in northwestern Scotland: new data to test existing models. Quaternary International 26, 97–123.
Stuiver, M., Pearson, G.W., Braziunas, T.F., 1986. Radiocarbon age calibration of marine samples back to 9000 cal. yr. bp. Radiocarbon 28 (2B), 980–1021.
Tushingham, A.M., Peltier, W.R., 1991. ICE-3G: a new global model of late Pleistocene deglaciation based on geophysical predictions of post-glacial relative sea level change. Journal of Geophysical Research 96, 4497–4523.
Vening Meinesz, F.A., 1937. The determination of the earth's plasticity from the post-glacial uplift of Scandinavia: isostatic adjustment. Koninklijke Akademie van Weten-schapen 40, 654–662.
Walcott, R.I., 1972. Past sea levels, eustasy and deformation of the Earth. Quaternary Research 2, 1–14.
Wieczerkowski, K., Mitrovica, J.X., Wolf, D., 1999. A revised relaxation-time spectrum for Fennoscandia. Geophysical Journal International 139, 69–86.
Woodward, R.S., 1888. On the form and position of mean sea level. United States Geological Survey Bulletin 48, 87–170.
Wu, P., Peltier, W.R., 1983. Glacial isostatic adjustment and the free air gravity anomaly as a constraint on deep mantle viscosity. Geophysical Journal of the Royal Astronomical Society 74, 377–449.
Wu, P., Peltier, W.R., 1984. Pleistocene deglaciation and the Earth's rotation: a new analysis. Geophysical Journal of the Royal Astronomical Society 76, 753–791.
Wu, P., 1999. Modelling postglacial sea levels with power-law rheology and a realistic ice model in the absence of ambient tectonic stress. Geophysical Journal International 139, 691–702.
Yokoyama, Y., Lambeck, K., De Deckker, P., Johnston, P., Fifield, L.K., 2000. Timing of the Last Glacial Maximum from observed sea-level minima. Nature 406, 713–716.